Author(s): Rossi, Tuomas P.; Kuisma, Mikael; Puska, Martti J.; Nieminen, Risto M.; Erhart, Paul

Title: Kohn-Sham Decomposition in Real-Time Time-Dependent Density-Functional Theory : An Efficient Tool for Analyzing Plasmonic Excitations

Year: 2017

Version:

Please cite the original version:

Rossi, T. P., Kuisma, M., Puska, M. J., Nieminen, R. M., & Erhart, P. (2017). Kohn-Sham Decomposition in Real-Time Time-Dependent Density-Functional Theory : An Efficient Tool for Analyzing Plasmonic Excitations. Journal of Chemical Theory and Computation, 13(10), 4779-4790. https://doi.org/10.1021/acs.jctc.7b00589

JCTC Journal of Chemical Theory and Computation

Article

Kohn–Sham decomposition in real-time time-dependent density-functional theory: An efficient tool for analyzing plasmonic excitations

Tuomas P. Rossi, Mikael Kuisma, Martti J. Puska, Risto M. Nieminen, and Paul Erhart

J. Chem. Theory Comput., **Just Accepted Manuscript** • DOI: 10.1021/acs.jctc.7b00589 • Publication Date (Web): 01 Sep 2017

ACS Publications

Journal of Chemical Theory and Computation is published by the American Chemical Society. 1155 Sixteenth Street N.W., Washington, DC 20036

Kohn–Sham decomposition in real-time time-dependent density-functional theory: An efficient tool for analyzing plasmonic excitations

Tuomas P. Rossi,*,† Mikael Kuisma,*,‡,¶ Martti J. Puska,† Risto M. Nieminen,† and Paul Erhart*,‡

†*COMP Centre of Excellence, Department of Applied Physics, Aalto University School of Science, Espoo, Finland*

‡*Department of Physics, Chalmers University of Technology, Gothenburg, Sweden*

¶*Department of Chemistry, Nanoscience Center, University of Jyväskylä, Jyväskylä, Finland*

E-mail: tuomas.rossi@alumni.aalto.fi; mikael.j.kuisma@jyu.fi; erhart@chalmers.se

Abstract

Electronic excitations can be efficiently analyzed in terms of the underlying Kohn–Sham (KS) electron-hole transitions. While such a decomposition is readily available in the linear-response time-dependent density-functional theory (TDDFT) approaches based on the Casida equations, a comparable analysis is less commonly conducted within the real-time-propagation TDDFT (RT-TDDFT). To improve this situation, we present here an implementation of a KS decomposition tool within the local-basis-set RT-TDDFT code in the free GPAW package. Our implementation is based on post-processing of data that is readily available during time propagation, which is impor-

tant for retaining the efficiency of the underlying RT-TDDFT to large systems. After benchmarking our implementation on small benzene derivatives by explicitly reconstructing the Casida eigenvectors from RT-TDDFT, we demonstrate the performance of the method by analyzing the plasmon resonances of icosahedral silver nanoparticles up to Ag_{561}. The method provides a clear description of the splitting of the plasmon in small nanoparticles due to individual single-electron transitions as well as the formation of a distinct *d*-electron-screened plasmon resonance in larger nanoparticles.

1 Introduction

Time-dependent density-functional theory (TDDFT)[1] built on top of Kohn–Sham (KS) density-functional theory (DFT)[2,3] is a powerful tool in computational physics and chemistry for accessing the optical properties of matter.[4,5] Starting from seminal works on jellium nanoparticles,[6–8] TDDFT has become a standard tool for modeling plasmonic response from a quantum-mechanical perspective,[9,10] and proven to be useful for calculating the response of individual nanoparticles,[11–21] and their compounds[22–32] as well as other plasmonic materials.[33–36] Additionally, a number of models and concepts have been developed for quantifying and understanding plasmonic character within the TDDFT framework.[37–48] Thus, in conjunction with other theoretical and computational methods[49–56] and experimental developments,[57–68] TDDFT is a valuable tool for understanding quantum effects within the nanoplasmonics field.[69,70] Recent methodological advances and a steady increase in computational power have extended the system size that can be treated at the TDDFT level, enabling the computational modeling of plasmonic phenomena in noble metal nanoparticles of several nanometers in diameter.[71–75]

TDDFT in the linear-response regime is often formulated in frequency space[76,77] in terms of the Casida matrix expressed in the Kohn–Sham electron-hole space.[76,78] The calculations are commonly performed by diagonalizing the Casida matrix directly or by solving the equivalent problem with different iterative subspace algorithms.[79–82] The real-time-propagation

formulation of TDDFT (RT-TDDFT)[83,84] is a computationally efficient alternative with favorable scaling with respect to system size,[85] and it is furthermore applicable to the non-linear regime.

The Casida approach directly enables a decomposition of the electronic excitations into the underlying KS electron-hole transitions, which readily yields quantum-mechanical understanding of the plasmonic response.[39–44,73,74,86,87] By contrast, RT-TDDFT results are often limited to absorption spectra or the analysis of induced densities or fields. Accordingly the lack of KS decomposition tools has been identified as a limitation of RT-TDDFT implementations.[73,74,85,88] While RT-TDDFT results can be analyzed, for example, by fitting KS transition densities to induced densities[89] or by considering time-dependent transition coefficients[45–47,90–92] or occupation numbers,[93–96] a natural way for obtaining a KS decomposition is to consider the full time-dependent Kohn–Sham density matrix in the KS electron-hole space.[97,98] Although such analysis in terms of KS transition coefficients arises naturally in the linear-response TDDFT, spatial analyses of the contributions can also be useful for obtaining complementary information.[99–101]

In this work, we present an implementation of a KS decomposition tool based on the RT-TDDFT code[72] that is available in the free GPAW package.[102–104] The underlying RT-TDDFT code uses the linear combination of atomic orbitals (LCAO) method[105] and enables calculations involving hundreds of noble metal atoms.[72] Our approach is based on the linear-response of the KS density matrix in the KS electron-hole space.[97,98] In our implementation, the relevant quantities are readily available and recorded during time propagation. After the simulation has completed, the KS decomposition can be constructed for the frequencies of interest. In particular, this implies that it is not necessary to define regions or features of possible interest *before* the time propagation.

We benchmark the numerical accuracy of our implementation on small benzene derivatives by explicitly reconstructing the Casida eigenvectors from RT-TDDFT. For such a benchmark, the GPAW code is advantageous since it provides RT-TDDFT and Casida approaches

on an equal footing, minimizing numerical error sources.

The primary application area of our implementation is in large-scale systems where the favorable size scaling of RT-TDDFT is beneficial. We demonstrate the applicability of the method to this class of problems by performing a KS decomposition analysis of plasmon formation in a series of icosahedral silver nanoparticles comprising Ag_{55}, Ag_{147}, Ag_{309}, and Ag_{561}. We observe that in the small Ag_{55} nanoparticle individual single-electron transitions still have a strong effect on the plasmonic response and cause the splitting of the plasmon resonance.[106–109] In Ag_{147} and larger nanoparticles, however, a distinct plasmon resonance is formed by the constructive coupling of low-energy single-electron transitions.[110,111] Here, the analysis also illustrates the important role of d-electrons in screening the plasmon.[112–114]

The structure of the article is as follows. In Sec. 2 we discuss the linear response of the time-dependent KS density matrix in the KS electron-hole space and review the formulation of the same quantity in the Casida approach. Additionally, we describe the decomposition of the photo-absorption spectrum in KS electron-hole contributions. In Sec. 3 we benchmark the numerical accuracy our RT-TDDFT implementation against the Casida method, and analyze the plasmonic response of the silver nanoparticles. In Sec. 4 we discuss the general features of the presented methodology. Our work is concluded in Sec. 5.

2 Methods

2.1 Linear response of the Kohn–Sham density matrix in the real-time propagation method

The time-dependent Kohn–Sham equation is defined as

$$i\frac{\partial}{\partial t}\psi_n(\boldsymbol{r},t) = H_{\mathrm{KS}}(t)\psi_n(\boldsymbol{r},t), \tag{1}$$

where $H_{\mathrm{KS}}(t)$ is the time-dependent KS Hamiltonian and $\psi_n(\boldsymbol{r},t)$ is a KS wave function. The KS density matrix operator is defined as

$$\rho(t) = \sum_n |\psi_n(t)\rangle\, f_n\, \langle\psi_n(t)|\,, \tag{2}$$

where f_n is an occupation factor of the nth KS state. In order to proceed with KS decomposition, we express the density matrix in the KS basis, spanned by the ground-state KS orbitals $\psi_n^{(0)}(\boldsymbol{r})$, which fulfill the ground-state KS equation

$$H_{\mathrm{KS}}^{(0)}\psi_n^{(0)}(\boldsymbol{r}) = \epsilon_n\psi_n^{(0)}(\boldsymbol{r}), \tag{3}$$

where $H_{\mathrm{KS}}^{(0)}$ is the ground-state KS Hamiltonian and ϵ_n the KS eigenvalue of nth state. The KS density matrix can be written in this KS basis as

$$\begin{aligned}\rho_{nn'}(t) &= \langle\psi_n^{(0)}|\rho(t)|\psi_{n'}^{(0)}\rangle \\ &= \sum_m \langle\psi_n^{(0)}|\psi_m(t)\rangle\, f_m\, \langle\psi_m(t)|\psi_{n'}^{(0)}\rangle\,. \end{aligned}\tag{4}$$

This equation establishes a link between a time-dependent density matrix and the usual KS (electron-hole) basis set used in linear-response calculations, see Sec. 2.2. Such a basis transformation of the KS density matrix has previously been shown to be useful for analyzing the decomposition of electronic excitations.[97,98]

When the real-time propagation method is applied in the linear-response regime, the usual approach is to use a δ-pulse perturbation.[83,84] This corresponds to the Hamiltonian

$$H_{\mathrm{KS}}(t) = H_{\mathrm{KS}}^{(0)} + zK_z\delta(t), \tag{5}$$

where the interaction with external electromagnetic radiation is taken within the dipole approximation. The electric field is assumed to be aligned along the z direction and the

constant K_z is proportional to the external electric field strength, which is assumed to be small enough to induce only negligible non-linear effects. After the perturbation by the δ-pulse at $t = 0$, Eq. (1) is propagated in time and the quantities of interest are recorded during the propagation. As a post-processing step, time-domain quantities, such as $\rho_{nn'}(t)$, can be Fourier transformed into the frequency domain.

It is important to note that the size of the density matrix $\rho_{nn'}(t)$ can be significantly reduced since only its electron-hole part is required in the linear-response theory.[76,78] It is thus sufficient to consider only $\rho_{ia}(t)$, where i and a represent occupied and unoccupied KS states, respectively. Then, we obtain the linear response of the KS density matrix in the electron-hole space as

$$\delta\rho^z_{ia}(\omega) = \frac{1}{K_z}\int_0^\infty \left[\rho^z_{ia}(t) - \rho_{ia}(0^-)\right] e^{i\omega t}\mathrm{d}t + \mathcal{O}(K_z), \tag{6}$$

where $\rho_{ia}(0^-)$ is the initial density matrix before the δ-pulse perturbation and the superscript z indicates the direction of the perturbation. Note that in Eq. (6), the response is already normalized with the perturbation strength K_z [see Eq. (5)].

In common TDDFT implementations, there is no mechanism for energy dissipation and the lifetime of excitations is infinite. A customary way to restore a finite lifetime is to apply the substitution $\omega \to \omega + i\eta$, where the parameter η is small. This leads to an exponentially decaying term in the integrand in Eq. (6), *i.e.*, $e^{i\omega t} \to e^{i\omega t}e^{-\eta t}$, and to the Lorentzian line shapes in the frequency domain. The decaying integrand also means that a finite propagation time is sufficient in practical calculations. The Gaussian line shapes can be obtained by replacing the Lorentzian decay $e^{-\eta t}$ with the Gaussian decay function $e^{-(\sigma t)^2/2}$, where the parameter σ determines the spectral line width.

Implementation

We have implemented the density matrix formalism outlined above in the RT-TDDFT code[72] that is a part of the free GPAW package,[102–104] utilizing the ASE library.[115,116] Our implementation uses the LCAO basis set[105] and the projector-augmented wave (PAW)[117] method. In the LCAO method the wave function $\psi_n(\boldsymbol{r}, t)$ is expanded in localized basis functions $\phi_\mu(\boldsymbol{r})$ centered at atomic coordinates

$$\psi_n(\boldsymbol{r}, t) = \sum_\mu \phi_\mu(\boldsymbol{r}) C_{\mu n}(t) \tag{7}$$

with expansion coefficients $C_{\mu n}(t)$. The KS density matrix in the LCAO basis set is

$$\rho_{\mu\nu}(t) = \sum_n C_{\mu n}(t) f_n C^*_{\nu n}(t). \tag{8}$$

Then, Eq. (4) can be written in LCAO formalism as (using implied summation over repeated indices)

$$\rho_{nn'}(t) = C^{(0)*}_{\mu n} S_{\mu\mu'} \rho_{\mu'\nu'}(t) S^*_{\nu\nu'} C^{(0)}_{\nu n'}, \tag{9}$$

where $S_{\mu\mu'} = \int \phi^*_\mu(\boldsymbol{r}) \phi_{\mu'}(\boldsymbol{r}) \mathrm{d}\boldsymbol{r}$ is the overlap integral of the basis functions. A detailed derivation of Eq. (9) is given in Supporting Information, in which it is shown that the PAW transformation affects only the evaluation of the overlap integral.

The emphasis in our implementation is to minimize the computational footprint of the analysis method in order to retain the performance of the underlying RT-TDDFT code. Thus, instead of calculating Eq. (9) at every time step during the time propagation, we do the basis set transformation as a post-processing step.

During the propagation, we store the matrix $C^z_{\mu n}(t)$ that is already available, and after the simulation has completed, we calculate $\rho^z_{\mu\nu}(t)$ via Eq. (8) [alternatively, $\rho^z_{\mu\nu}(t)$ could be directly stored during the propagation]. The density matrix in the LCAO basis set is Fourier transformed analogously to Eq. (6) to obtain $\delta\rho^z_{\mu\nu}(\omega)$, which is subsequently transformed to

the Kohn–Sham basis as

$$\delta\rho^z_{nn'}(\omega) = C^{(0)*}_{\mu n} S_{\mu\mu'} \delta\rho^z_{\mu'\nu'}(\omega) S^*_{\nu\nu'} C^{(0)}_{\nu n'}, \tag{10}$$

which is analogous to Eq. (9). By keeping only the electron-hole part in Eq. (10), $\delta\rho^z_{ia}(\omega)$ is obtained. Thus, in practice, the linearity of the equations allows exchanging the order of the Fourier transformation and matrix multiplications, and the basis set transformation needs to be evaluated only for the chosen frequencies.

In our experience it is advantageous to store the whole time-dependent evolution of the system, *i.e.*, $C^z_{\mu n}(t)$ or $\rho^z_{\mu\nu}(t)$, as is done in the present implementation. The main drawback of this approach is that the disk space requirements can be large, though not insuperable in a modern supercomputing environment. If necessary, the disk space requirements can, however, be significantly reduced by, *e.g.*, filtering out the high-frequency components of $\rho^z_{\mu\nu}(t)$, when they are of no interest. Further reduction in required disk space could be obtained by calculating the Fourier transformation $\delta\rho^z_{\mu\nu}(\omega)$ already during the propagation. However, a major disadvantage of such an on-the-fly Fourier transformation is that it would restrict the analysis to the set of frequencies and Gaussian/Lorentzian broadening parameters specified at the outset of the calculation.

2.2 Linear response of the Kohn–Sham density matrix in the Casida method

In Casida's linear-response formulation of TDDFT[76,78] the response is obtained by solving the matrix eigenvalue equation

$$\mathbf{\Omega}\mathbf{F}_I = \omega_I^2 \mathbf{F}_I \tag{11}$$

yielding excitation energies ω_I and corresponding Casida eigenvectors $\mathbf{F}_I$. The matrix $\mathbf{\Omega}$ is constructed in the KS electron-hole space. Using a double-index ia (jb) to denote a KS excitation from an occupied state i (j) to an unoccupied state a (b), the elements of the

matrix can be written as

$$\Omega_{ia,jb} = \omega_{ia}^2 \delta_{ia,jb} + 2\sqrt{f_{ia}\omega_{ia}} K_{ia,jb} \sqrt{f_{jb}\omega_{jb}}, \tag{12}$$

where $f_{ia} = f_i - f_a$ is the occupation number difference, $\omega_{ia} = \epsilon_a - \epsilon_i$ is the KS eigenvalue difference, see Eq. (3), and the matrix $K_{ia,jb}$ represents the coupling between the excitations $i \to a$ and $j \to b$.[76]

The linear response of the KS density matrix at frequency ω can be obtained as[76]

$$\delta\rho_{ia}^z(\omega) = \sqrt{f_{ia}\omega_{ia}} \sum_I F_{I,ia} G_I(\omega) \sum_{jb}^{\text{eh}} F_{I,jb}^* \sqrt{f_{jb}\omega_{jb}} \mu_{jb}^z. \tag{13}$$

where $\mu_{jb}^z = \int \psi_j^{(0)*}(\boldsymbol{r}) z \psi_b^{(0)}(\boldsymbol{r})\, \mathrm{d}\boldsymbol{r}$ is the dipole matrix element and the summation runs over electron-hole pairs (eh). Here $G_I(\omega) = 1/(\omega^2 - \omega_I^2)$ originates from the spectral decomposition $(\omega^2 \mathbf{1} - \mathbf{\Omega})^{-1}_{ia,jb} = \sum_I F_{I,ia} G_I(\omega) F^*_{I,jb}$.[76]

The term $G_I(\omega)$ is divergent at excitation energies ω_I in the common TDDFT implementations due to the infinite lifetime of the excitations. Analogously to the time domain, a finite lifetime for the excitations can be restored by the substitution $\omega \to \omega + i\eta$, where the arbitrary parameter η determines the lifetime. This leads to a Lorentzian line shape and the imaginary part is given by

$$\mathrm{Im}\left[G_I(\omega)\right] = \frac{\pi}{2\omega_I}\left[L(\omega) - L(-\omega)\right], \tag{14}$$

where $L(\omega) = 1/\pi \cdot \eta/[(\omega - \omega_I)^2 + \eta^2]$ is the Lorentzian function. Alternatively, the Gaussian line shape can be obtained by using the Gaussian function $g(\omega) = 1/\sqrt{2\pi}\sigma \cdot \exp[-(\omega - \omega_I)^2/2\sigma^2]$ instead of the Lorentzian function $L(\omega)$ in Eq. (14).

2.3 Kohn–Sham decomposition

The linear response of the KS density matrix in the KS electron-hole space, $\delta\rho^z_{ia}(\omega)$, can be calculated equivalently using both the real-time propagation [Eq. (6)] and the Casida approach [Eq. (13)]. While this quantity would already allow the analysis of the response at frequency ω in terms of its components in the KS electron-hole space, a more intuitive analysis can be obtained by connecting $\delta\rho^z_{ia}(\omega)$ to an observable photo-absorption cross-section describing the resonances of the system. First, the dynamical polarizability is given by

$$\alpha_{xz}(\omega) = -2\sum_{ia}^{\mathrm{eh}} \mu^{x*}_{ia}\delta\rho^z_{ia}(\omega), \tag{15}$$

where the negative sign incorporates the electron charge.[76] The photo-absorption is described by the dipole strength function

$$S_z(\omega) = \frac{2\omega}{\pi}\mathrm{Im}\left[\alpha_{zz}(\omega)\right], \tag{16}$$

which is normalized to integrate to the number of electrons in the system N_e, *i.e.*, $\int_0^\infty S_z(\omega)\mathrm{d}\omega = N_e$. This is similar to the sum rule $\sum_I f^z_I = N_e$, where $f^z_I = 2\left|\sum_{ia}\mu^{z*}_{ia}\sqrt{f_{ia}\omega_{ia}}F_{I,ia}\right|^2$ is the z-component of the oscillator strength of the discrete excitation I.[76,118]

By comparing Eqs. (15) and (16), we can now define the KS decomposition of the absorption spectrum as

$$S^z_{ia}(\omega) = -\frac{4\omega}{\pi}\mathrm{Im}\left[\mu^{z*}_{ia}\delta\rho^z_{ia}(\omega)\right]. \tag{17}$$

Similar photo-absorption decompositions have been used in the electron-hole space[97,98] and based on, *e.g.*, spatial location[75,101] or angular momentum.[75]

Once the relevant KS transitions of a resonance have been recognized, their real-space induced density contributions to the resonance can be analyzed. The density contribution

from the transition $i \to a$ is given by

$$\delta n^z_{ia}(\boldsymbol{r},\omega) = 2\psi^{(0)}_i(\boldsymbol{r})\psi^{(0)*}_a(\boldsymbol{r})\delta\rho^z_{ia}(\omega), \tag{18}$$

where $\psi^{(0)}_i(\boldsymbol{r})$ and $\psi^{(0)}_a(\boldsymbol{r})$ are the occupied (i) and unoccupied (a) ground-state KS orbitals corresponding to the transition, respectively. Eq. (17) can be expressed in terms of $\delta n^z_{ia}(\boldsymbol{r},\omega)$ as $S^z_{ia}(\omega) = -2\omega/\pi \cdot \int z\,\mathrm{Im}\left[\delta n^z_{ia}(\boldsymbol{r},\omega)\right]\mathrm{d}\boldsymbol{r}$. Thus, analogously to the photo-absorption, the imaginary part $\mathrm{Im}[\delta n]$ describes the resonant response. The density contributions sum up to the total induced electron density $\delta n^z(\boldsymbol{r},\omega) = \sum^{\mathrm{eh}}_{ia} \delta n^z_{ia}(\boldsymbol{r},\omega)$. Eqs. (17) and (18) are used for analyzing the response of silver nanoparticles in Sec. 3.2 below.

3 Results

3.1 Benzene derivatives

To benchmark the presented methods and their computational implementation, we now analyze the optical response of the molecular systems benzene (C_6H_6), naphthalene ($C_{10}H_8$), and anthracene ($C_{14}H_{10}$) using both the RT-TDDFT and Casida implementations in GPAW package.[102–104,119] These characteristic conjugated molecules are suited for the present benchmark as they have well-defined $\pi \to \pi^*$ transitions that exhibit a systematic red-shift as the extent of the conjugated π-system increases.[120,121]

As the real-time propagation uses the full time-dependent Hamiltonian matrices, the end result includes contributions from all electron-hole pairs and the limit of the full KS space is automatically achieved by propagating only the occupied orbitals. This is in contrast to the GPAW implementation of the Casida approach,[119] which commonly requires setting an energy cut-off that determines the KS transitions included in the calculation of the Casida matrix. In order to ensure the comparability of the results, we have included in the calculation of the Casida matrix all the transitions that are possible within the KS electron-hole space spanned

by the orbitals.

Both the RT-TDDFT and Casida calculations were carried out using the default PAW data sets and the default double-ζ polarized (dzp) basis sets within the LCAO description. While these dzp basis sets might not be sufficient for yielding numerical values at the complete-basis-set limit,[105,122] they are suitable for qualitative analyses and for the benchmarking study presented here. The Perdew-Burke-Ernzerhof (PBE)[123] exchange-correlation functional was employed in the adiabatic limit. A coarse grid spacing of 0.3 Å was chosen to represent densities and potentials and the molecules were surrounded by a vacuum region of at least 6 Å. The Hartree potential was evaluated with a multigrid Poisson solver using the monopole and dipole corrections for the potential.

For the RT-TDDFT calculations, we used a small time step of $\Delta t = 5\,\text{as}$ in order to achieve high numerical accuracy. The total propagation time was $T = 30\,\text{fs}$, which is sufficient for the used Gaussian broadening with $\sigma = 0.07\,\text{eV}$ corresponding to a full width at half-maximum (FWHM) of 0.16 eV.

The calculated photo-absorption spectra of the benzene derivatives are shown in Fig. 1. The Casida and RT-TDDFT methods yield virtually indistinguishable spectra. For conciseness, we only present an analysis for excitations along the long axis (x) of the molecules. Note, however, that the response in the other directions can be analyzed in similar fashion.

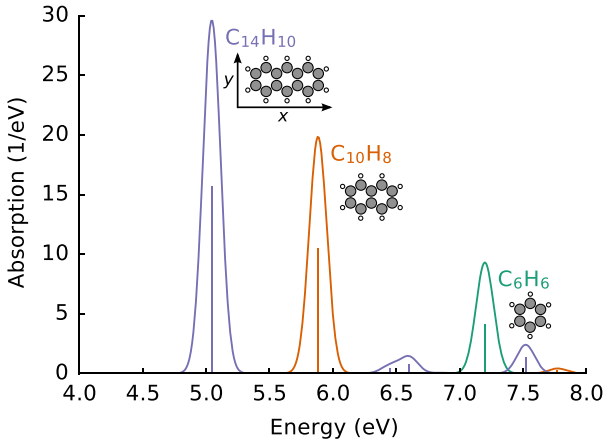

Figure 1: Photo-absorption spectra $S_x(\omega)$ along the long axis (x) of the benzene derivatives.

Table 1: Casida analysis of the most prominent excitations of benzene (C_6H_6), naphthalene ($C_{10}H_8$), and anthracene ($C_{14}H_{10}$). Orbitals are enumerated with respect to HOMO (π_{-0}) and LUMO (π^*_{+0}). The orbital characters are given in brackets based on the point groups D_{6h} (benzene) and D_{2h} (naphthalene, anthracene).

Molecule	ω_I (eV)	f_I^x	$i \to a$	$F^2_{I,ia}$
C_6H_6	7.198	0.2784	$\pi_{-1}(E_{1g}) \to \pi^*_{+1}(E_{2u})$	0.31430
			$\pi_{-0}(E_{1g}) \to \pi^*_{+0}(E_{2u})$	0.31254
			$\pi_{-1}(E_{1g}) \to \pi^*_{+0}(E_{2u})$	0.16863
			$\pi_{-0}(E_{1g}) \to \pi^*_{+1}(E_{2u})$	0.16833
	7.199	1.3546	$\pi_{-1}(E_{1g}) \to \pi^*_{+0}(E_{2u})$	0.31362
			$\pi_{-0}(E_{1g}) \to \pi^*_{+1}(E_{2u})$	0.31325
			$\pi_{-1}(E_{1g}) \to \pi^*_{+1}(E_{2u})$	0.16895
			$\pi_{-0}(E_{1g}) \to \pi^*_{+0}(E_{2u})$	0.16793
$C_{10}H_8$	5.883	3.4839	$\pi_{-0}(A_u) \to \pi^*_{+1}(B_{3g})$	0.48451
			$\pi_{-1}(B_{2u}) \to \pi^*_{+0}(B_{1g})$	0.47748
$C_{14}H_{10}$	5.044	5.2000	$\pi_{-0}(B_{3g}) \to \pi^*_{+1}(A_u)$	0.50237
			$\pi_{-1}(B_{2g}) \to \pi^*_{+0}(B_{1u})$	0.45773
			$\pi_{-4}(B_{1u}) \to \pi^*_{+2}(B_{2g})$	0.01049

Casida approach

The response of each of the molecules is dominated by a single absorption peak (see Fig. 1), which results from discrete excitations. In Table 1, we show the KS decomposition of these excitations as described by the components of the normalized Casida eigenvectors $F_{I,ia}$. Due to the normalization, $\sum_{ia} F^2_{I,ia} = 1$ for each excitation I.

For benzene (C_6H_6, point group D_{6h}) the excitation at 7.2 eV corresponds to the first E_{1u} transition from the doubly degenerate highest occupied molecular orbital (HOMO; E_{1g}) to the doubly degenerate lowest unoccupied molecular orbital (LUMO; E_{2u}). In the present calculations the symmetry of the molecule has not been enforced and the orbitals $\pi_{-0/1}$ and $\pi^*_{+0/1}$ span the E_{1g} and E_{2u} symmetries, respectively. Implementation-dependent numerical factors slightly lift their degeneracy and determine the exact unitary rotation between the states.

Naphthalene ($C_{10}H_8$) and anthracene ($C_{14}H_{10}$) belong to the D_{2h} symmetry point group. In both molecules the most prominent excitation is the B_{3u} transition, which is mainly composed of transitions from HOMO to LUMO+1 and HOMO−1 to LUMO. While in naphtha-

Table 2: RT-TDDFT analysis at the peak energies ω of benzene (C_6H_6), naphthalene ($C_{10}H_8$), and anthracene ($C_{14}H_{10}$). The intensities $S_x(\omega)$ have been multiplied with the area under the peak to facilitate a comparison with the oscillator strengths f_I^x shown in Table 1. The last column shows for reference $[F_{ia}^x(\omega)]^2$ as calculated with the Casida approach.

Molecule	ω (eV)	$S_x(\omega)$	$i \to a$	$[F_{ia}^x(\omega)]^2$	Casida
C_6H_6	7.20	1.6283	$\pi_{-1} \to \pi^*_{+0}$	0.46184	0.46186
			$\pi_{-0} \to \pi^*_{+1}$	0.46126	0.46126
			$\pi_{-1} \to \pi^*_{+1}$	0.02045	0.02043
			$\pi_{-0} \to \pi^*_{+0}$	0.02032	0.02030
$C_{10}H_8$	5.88	3.4776	$\pi_{-0} \to \pi^*_{+1}$	0.48472	0.48451
			$\pi_{-1} \to \pi^*_{+0}$	0.47728	0.47748
$C_{14}H_{10}$	5.04	5.1903	$\pi_{-0} \to \pi^*_{+1}$	0.50277	0.50241
			$\pi_{-1} \to \pi^*_{+0}$	0.45745	0.45777
			$\pi_{-4} \to \pi^*_{+2}$	0.01044	0.01049

lene the other contributions amount to less than 1%, in anthracene, a minor contribution originates also from a transition from HOMO−4 to LUMO+2.

RT-TDDFT approach

The Casida eigenvector $F_{I,ia}$ considered in Table 1 is directly related to the linear response of the KS density matrix, see Eq. (13), and is employed here for benchmarking the RT-TDDFT methodology described Sec. 2.1. In order to proceed with comparison, consider a discrete excitation J that is energetically separated from other excitations. Since $\mathrm{Im}[G_I(\omega_J)]$ in Eq. (14) is approximately zero when $I \neq J$, only the excitation J contributes in Eq. (13). This implies that $\mathrm{Im}[\delta\rho_{ia}^x(\omega_J)] \approx A\sqrt{f_{ia}\omega_{ia}}F_{J,ia}$, where A is a constant independent of index ia. Thus, after normalization, $\mathrm{Im}[\delta\rho_{ia}^x(\omega_J)]/\sqrt{f_{ia}\omega_{ia}} \equiv F_{ia}^x(\omega_J)$ yields the components of the Casida eigenvector $F_{J,ia}$. This connection allows us to calculate the Casida eigenvector also from the RT-TDDFT approach. This is demonstrated in Table 2, in which we show the calculated KS decompositions at the peak energies of the photo-absorption spectrum (Fig. 1).

In the case of benzene (C_6H_6), we inevitably obtain a superposition of the two underlying degenerate excitations (see Table 1). We can, however, calculate the equivalent superimposed

$F^x_{ia}(\omega)$ eigenvector also from the Casida approach (shown in the last column of Table 2). For this quantity, we obtain an excellent match between the RT-TDDFT and Casida approaches.

For naphthalene ($C_{10}H_8$) and anthracene ($C_{14}H_{10}$), a single excitation dominates the response and $F^2_{I,ia}$ and $[F^x_{ia}(\omega)]^2$ should yield the same decomposition as discussed above. Indeed, we observe that the RT-TDDFT calculations of the decomposition $[F^x_{ia}(\omega)]^2$ reproduce the discrete Casida eigenvector $F^2_{I,ia}$ with very good numerical accuracy. When both $F^2_{I,ia}$ and $[F^x_{ia}(\omega)]^2$ are calculated with the Casida approach, their values should be identical if the excitation is completely isolated. While for naphthalene ($C_{10}H_8$), these quantities are exactly the same up to the shown number of digits (compare the last columns of Tables 1 and 2), for anthracene ($C_{14}H_{10}$), the numerical values differ slightly. This deviation is due to a small contribution from a weak excitation that is close in energy ($\omega_I = 5.051\,\mathrm{eV}$, $f^x_I = 5 \cdot 10^{-4}$) to the dominant excitation of the anthracene molecule.

3.2 Silver nanoparticles

TDDFT calculations of noble metal nanoparticles up to diameters of several nanometers are computationally demanding, but they have become feasible with recent developments.[71–75] Here, we focus on silver nanoparticles as prototypical nanoplasmonic systems with a strong plasmonic response in the visible–ultraviolet light regime.[58,59] Using the methodology described above in conjunction with the underlying RT-TDDFT implementation,[72] we can analyze the response of silver nanoparticles with reasonable computational resources. For illustration, a full real-time propagation of 3000 time steps for Ag_{561} can be realized in 110 hours using 144 cores on an Intel Haswell based architecture.[124]

Kuisma *et al.* have previously studied icosahedral silver nanoparticles composed of 55, 147, 309, and 561 atoms corresponding to diameters ranging from 1.1 nm to 2.7 nm.[72] Here, we consider the same nanoparticle series and use the same geometries and computational parameters as in ref 72. We employ optimized LCAO basis sets[72] and the orbital-dependent Gritsenko-van Leeuwen-van Lenthe-Baerends (GLLB)[125] exchange-correlation potential with

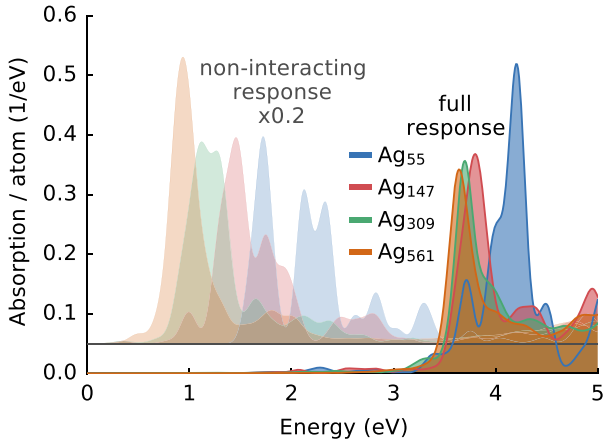

Figure 2: Photo-absorption spectra of icosahedral silver nanoparticles. The non-interacting-electron spectra shown for comparison are vertically shifted and scaled by a factor of 0.2.

the solid-state modification by Kuisma *et al.* (GLLB-SC),[126] which yields an accurate description of the d electron states in noble metals.[72,127,128]

The calculated photo-absorption spectra of the nanoparticles are shown in Fig. 2. The non-interacting-electron spectra calculated from the KS eigenvalue differences ω_{ia} and transition dipole matrix elements μ^x_{ia} are also shown to facilitate the discussion below. In ref 72 it was observed that the plasmon resonance is well-formed in Ag_{147} and in larger nanoparticles, whereas the response of Ag_{55} consists of multiple peaks, the origin of which could not be readily resolved. In the following, we analyze the response of nanoparticles in terms of the KS decomposition, which enables us to shed light on the response of the Ag_{55} nanoparticle.

Transition contribution maps

In order to analyze the response in terms of the Kohn–Sham decomposition, we present the decomposition as a transition contribution map (TCM; see Fig. 3 below),[40,129] which is an especially useful representation for plasmonic systems in which resonances are typically superpositions of many electron-hole excitations. The TCM represents the KS decomposition weight $w_{ia}(\omega)$ at a fixed ω in the two-dimensional (2D) $(\varepsilon_o, \varepsilon_u)$-plane spanned by the energy

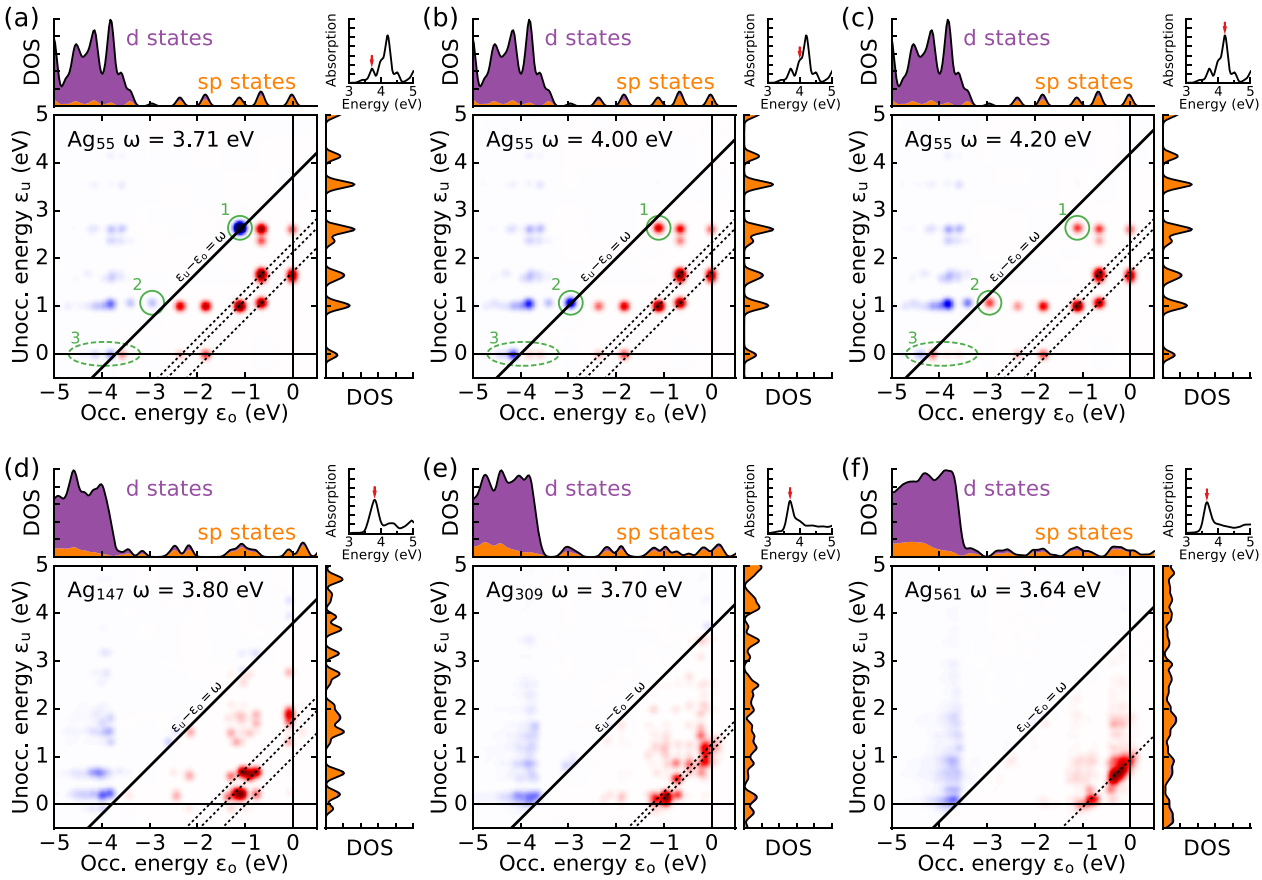

Figure 3: Transition contribution maps for the photo-absorption decomposition of Ag_{55} at different resonance energies ω (a–c), and those of Ag_{147} (d), Ag_{309} (e), and Ag_{561} (f) at the respective plasmon resonance energies. The KS eigenvalues are given with respect to the Fermi level. The constant transition energy lines $\varepsilon_u - \varepsilon_o = \omega$ are superimposed at the analysis energy (solid line) and at the resonance energies of the non-interacting-electron spectra (dashed lines, see Fig. 2). Red and blue colors indicate positive and negative values of the photo-absorption decomposition, respectively. The inset of each panel shows the absorption spectrum with the arrow pointing at the analysis frequency ω. The densities of states (DOS) have been colored to indicate *sp* and *d* character of the states. The transitions marked with green ellipses in panels (a–c) are discussed in the text.

axes for occupied and unoccupied states. More specifically, the 2D plot is defined by

$$M_\omega^{\mathrm{TCM}}(\varepsilon_o, \varepsilon_u) = \sum_{ia} w_{ia}(\omega) g_{ia}(\varepsilon_o, \varepsilon_u), \tag{19}$$

where g_{ia} is a 2D broadening function for the discrete KS $i \to a$ transition contributions. Here, we employ the 2D Gaussian function

$$g_{ia}(\varepsilon_{\mathrm{o}}, \varepsilon_{\mathrm{u}}) = \frac{1}{2\pi\sigma^2} \exp\left[-\frac{(\varepsilon_{\mathrm{o}} - \epsilon_i)^2 + (\varepsilon_{\mathrm{u}} - \epsilon_a)^2}{2\sigma^2}\right] \tag{20}$$

with $\sigma = 0.07\,\mathrm{eV}$ to give a finite size for each $i \to a$ contribution. The same σ parameter is also used in the spectral broadening. For the weight $w_{ia}(\omega)$, we use the absorption decomposition of Eq. (17) normalized by the total absorption, *i.e.*,

$$w_{ia}(\omega) = S^x_{ia}(\omega)/S_x(\omega). \tag{21}$$

Due to the icosahedral symmetry of the nanoparticles their response is isotropic, $S_x(\omega) = S_y(\omega) = S_z(\omega)$, and the decomposition is degenerate (compare to the case of benzene in Sec. 3.1).

Alternatively, instead of Eq. (21) one could use, *e.g.*, the normalized transition density matrix ($w_{ia}(\omega) = |\delta\rho^x_{ia}(\omega)|^2$) as the weight. Eq. (21), however, has the advantage that it retains the information about the sign of the response in the KS decomposition and has a physically sound interpretation as the photo-absorption decomposition.

TCMs of the nanoparticles at different resonance energies are shown in Fig. 3 along with the density of states (DOS), which has been colored to indicate the *sp* and *d* character of the states. The latter decomposition is based on the angular momentum quantum number l_μ of the LCAO basis functions indexed by μ. For example, the *d* character of the nth state is estimated as $\sum_{\mu:l_\mu=2} |C^{(0)}_{\mu n}|^2$, where the coefficients are normalized such that $\sum_\mu |C^{(0)}_{\mu n}|^2 = 1$.

Analysis of Ag_{147}, Ag_{309}, and Ag_{561}

First, we consider the largest nanoparticles Ag_{147}, Ag_{309}, and Ag_{561}, the TCMs of which are shown in Figs. 3(d–f). The TCMs highlight two major features in their response. First, there is a strong positive constructive contribution[41] (red features in Fig. 3) from the KS

transitions whose eigenvalue differences are significantly lower than the plasmon resonance energy ω.[111] The same low-energy *sp* transitions are responsible for the strong peaks in the non-interacting-electron spectra (see Fig. 2), which are indicated in Fig. 3 by dashed lines. Thus, TCM shows how the resonance energy is blue-shifted as the interaction is turned on from the non-interacting case ($\lambda = 0$) to the fully interacting one ($\lambda = 1$). This demonstrates the plasmonic nature of the excitation in the so-called λ-scaling approach for plasmon identification,[39,130] and illustrates the importance of low-energy transitions for plasmon formation.[47,111] Another prominent feature in the response is the damping due to *d* electrons,[112–114] which is seen in the TCMs as large negative contributions from occupied *d* states into unoccupied states (blue features at $\varepsilon_\mathrm{o} \approx -4\,\mathrm{eV}$ in Fig. 3). Interestingly, the plasmon peak appears close to the onset of *d* electron transitions, corresponding to the intersection of the line $\varepsilon_\mathrm{u} - \varepsilon_\mathrm{o} = \omega$ and the horizontal Fermi level line. Generally, with increasing nanoparticle size the DOS becomes increasingly continuous, which is also visible in the increasing uniformity of the TCMs.

Fig. 4 visualizes for Ag_{561} the real-space contributions of the low-energy KS transitions (with $\epsilon_a - \epsilon_i < 3\,\mathrm{eV}$; corresponding in the TCM to the region $\varepsilon_\mathrm{u} - \varepsilon_\mathrm{o} < 3\,\mathrm{eV}$) and *d* electron transitions (with $\epsilon_i < -3\,\mathrm{eV}$; in the TCM the region $\varepsilon_\mathrm{o} < -3\,\mathrm{eV}$) in panels (b) and (c), respectively. Such contributions are obtained via Eq. (18) by summing up the selected KS transitions. The full induced density in panel (a) is obtained by a sum over all the KS transitions. The low-energy *sp* contributions show clearly the localized surface plasmon resonance. The *d* electron transitions are seen as counter-polarized dipoles localized mostly at the atomic coordinates.[72]

In ref 74, TCMs for charged silver nanoparticles up to Ag_{309} have been studied. The two main features in Fig. 3, the low-energy *sp* transitions and the *d* electron damping, are in agreement with these TCMs reported earlier. In contrast to Fig. 3, the TCMs in ref 74 show, however, also a significant contribution from *sp* transitions close to the $\varepsilon_\mathrm{u} - \varepsilon_\mathrm{o} = \omega$ line. We consider this to be due to the different choice of the TCM weight $w_{ia}(\omega)$ in ref 74. In

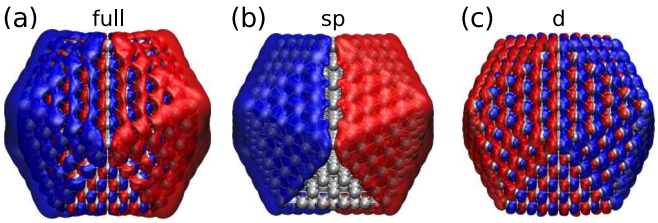

Figure 4: Visualization of Ag_{561} plasmon resonance. (a) Full and (b–c) partial induced densities $\mathrm{Im}[\delta n]$ at 3.64 eV. Positive (red) and negative (blue) isosurfaces are shown using the same isovalues in all the panels. Panel (b) includes KS transitions with $\omega_{ia} < 3\,\mathrm{eV}$ and panel (c) those with $\epsilon_i < -3\,\mathrm{eV}$.

the absorption decomposition we used in Fig. 3 [Eqs. (17) and (21)] the KS components are essentially weighted with the dipole matrix element μ^x_{ia}, which affects the relative magnitudes observed in TCM.

Analysis of Ag_{55}

Next, we consider the Ag_{55} nanoparticle that exhibits multiple strong peaks in the absorption spectrum, resulting in difficulties in identifying the plasmon resonance. The TCM analyses for the three prominent peak energies are shown in Figs. 3(a–c). Due to its small size, Ag_{55} has well separated, discrete KS states as is visible in its DOS. The overall features in TCMs are similar to those of the larger nanoparticles, *i.e.*, the low-energy *sp* transitions and the *d* electron transitions yield positive and negative contributions, respectively, though the low-energy transitions that form the plasmon are energetically clearly separated.

In contrast to the larger nanoparticles, in the Ag_{55} nanoparticle some of the strongly contributing *sp* transitions are located close to the peak frequencies, *i.e.*, close to the solid $\varepsilon_\mathrm{u} - \varepsilon_\mathrm{o} = \omega$ lines in the TCMs. These excitations are marked in Figs. 3(a–c) by green circles numbered as 1 and 2. By examining these KS transitions as a function of frequency ω (TCMs with the 0.01 eV resolution are provided in Supporting Information), we note that the first transition changes its sign at $\omega = 3.85\,\mathrm{eV}$, close to the minimum between the peak maxima at 3.71 eV [Fig. 3(a)] and 4.00 eV (b). Similarly, the second transition changes its sign at $\omega = 4.06\,\mathrm{eV}$ between the maxima at 4.00 eV (b) and 4.20 eV (c). At the same time, the

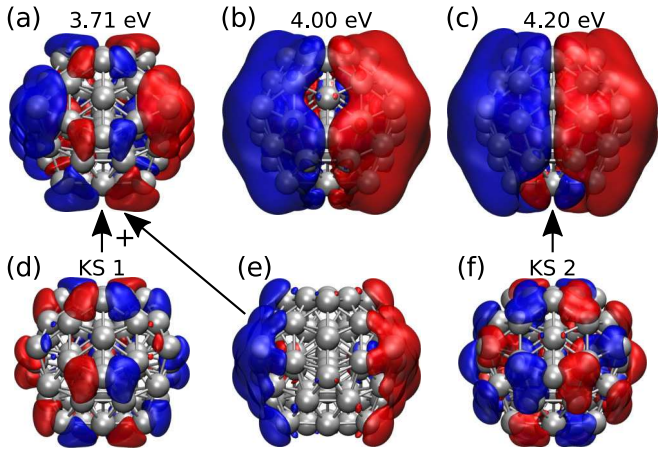

Figure 5: Visualization of Ag_{55} resonances. Induced density contributions from *sp* transitions ($\epsilon_i > -3\,\mathrm{eV}$) at (a) 3.71 eV, (b) 4.00 eV, and (c) 4.20 eV. In panels (d–e), the induced density of (a) is split into two parts: density contributions from (d) the KS transition numbered 1 and from (e) all the other *sp* transitions. Similarly, panel (f) shows the density contribution from the KS transition numbered 2 to the 4.20 eV resonance [panel (c)]. In panels (a–c) the isosurface values are 5% of the maxima. Panels (d–e) use the same isovalues as panel (a), and panel (f) the same as (c).

low-energy transitions forming the plasmon remain mainly unchanged over this frequency window. Thus, the presence of multiple peaks in the Ag_{55} spectrum seems to correspond to a strong coupling between the marked KS transitions and the plasmon. This is seen as the splitting (or fragmentation) of the plasmon into multiple resonances[106–109] with antisymmetric and symmetric combinations of the KS transition and the plasmonic transitions. The resulting resonances at 3.71 eV and 4.00 eV have relatively strong contributions from the corresponding individual KS transitions, *i.e.*, they have single-particle character in this respect. However, the positive contribution to the resonances originates from the lower-energy transitions forming the plasmon. In the larger nanoparticles, the interaction between the plasmon and the nearby KS transitions is weak and the coupling is merely seen as a broadening of the plasmon peak.[111]

Further insight can be obtained by considering the real-space shapes of the strongly contributing KS transitions. The induced density contributions from the KS transitions with $\epsilon_i > -3\,\mathrm{eV}$ (*sp* transitions; corresponding in the TCM to the region $\varepsilon_\mathrm{o} > -3\,\mathrm{eV}$) are shown in Figs. 5(a–c) for the different resonance energies. The contributions from the

KS transitions numbered 1 and 2 are shown in panels (d) and (f) for 3.71 eV and 4.20 eV resonances, respectively. These transition densities are of the same spatial shape at all energies, but their signs and relative strengths are different at different resonances following the corresponding values in the TCMs. Both of the transitions are delocalized over the nanoparticle, which allows them to couple strongly with the other delocalized low-energy KS transitions forming the plasmon. This is illustrated for the 3.71 eV resonance in panels (d–e). The total response [panel (a)] is composed of an emerging surface contribution from the low-energy transitions [panel (e)], which is disturbed by a destructive contribution from the single KS transition [panel (d)]. At the higher 4.00 eV and 4.20 eV resonances these two contributions are constructively coupled leading to a smoother surface density [panels (b–c)]. For these two higher resonances, the second KS transition [panel (f)] couples either destructively (4.00 eV) or constructively (4.20 eV).

A detailed inspection reveals that some *d* electron transitions also change their sign in the frequency range where the peak splitting occurs. These transitions are marked in Figs. 3(a–c) by a dashed green ellipse with the number 3. The changes in their sign, however, do not match the maxima and minima of the absorption spectrum as in the case of the marked KS transitions. Thus, we expect the indicated *sp* transitions to be the major cause for the plasmon splitting.

In the literature, Ag_{55} has been reported to have slightly varying spectra depending, *e.g.*, on the exact geometry, the exchange-correlation functional, and the numerical parameters used.[14,47,74,75,122,131,132] Correspondingly, the Ag_{55} spectra have single or multiple peaks depending on the exact electronic structure and the alignment of the discrete KS states.

4 Discussion

The RT-TDDFT approach provides more favorable scaling with the system size than the Casida approach. The latter, however, achieves a smaller pre-factor, especially when using

non-local (*e.g.*, hybrid) exchange-correlation functionals,[85] which renders it computationally more efficient for small and moderately-sized systems. In contrast, the RT-TDDFT approach becomes very attractive for systems comprising thousands of electrons (and typically hundreds of atoms) such as the silver nanoparticles considered in the present work.

It should be noted that in the RT-TDDFT approach the observable response is sensitive to the external perturbation used to initialize the time propagation. If the perturbation is chosen to be, say, a dipole perturbation along the x direction, only the excitations with a dipole component parallel to x are observable in the response. By combining at most three separate time-propagation calculations (possibly even less in the cases of higher symmetry) with dipole perturbations along the x, y, and z axes, one can recover the full dynamical polarizability tensor. However, for obtaining optically dark (dipole-forbidden) excitations from RT-TDDFT calculations, one would need to run the time propagation with different initial perturbations. This is in contrast to the Casida approach, where also dipole-forbidden excitations are obtained by diagonalizing the $\mathbf{\Omega}$ matrix.

It was illustrated in Sec. 3.1 that the presented method does not yield direct access to the discrete spectrum, but rather allows an analysis at chosen frequencies yielding the combined response coming from all the contributing discrete excitations. Usually, this is not a significant restriction as in experimental measurements the energy resolution is limited by instrumental broadening and the excitation lifetimes. Computationally, when a Fourier transform is used as in Eq. (6), the energy resolution is determined by the broadening parameter, which can be always reduced by increasing the propagation time. Alternatively, fitting approaches can be beneficial for accessing the underlying discrete response with reduced propagation time.[98] However, for larger systems that are the primary application area for RT-TDDFT, the electronic spectrum becomes increasingly dense and the distinction of individual excitations is less relevant.

5 Conclusions

In this work, we have presented an implementation of a Kohn–Sham decomposition analysis tool in RT-TDDFT. The tool is combined with a recent RT-TDDFT code[72] and is to be made publicly available as a part of the free electronic structure code GPAW.[102–104] In our implementation, the efficiency of the underlying RT-TDDFT code is retained and the analysis is performed as a post-processing step from the data that is recorded during the time propagation. Thus, all the analysis, including the transition contribution maps as well as the full and partial induced densities, can be obtained after the time propagation, without *a priori* knowledge or guesses of the interesting frequencies or KS transitions for the system in consideration.

The present approach yields orbital assignments of electronic excitations on par with the Casida method. This was specifically demonstrated by a careful comparison of the results for benzene derivatives, which were shown to be numerically almost identical for Casida and RT-TDDFT calculations.

The performance of the approach and implementation was further demonstrated by analyzing plasmon resonances in icosahedral silver nanoparticles up to Ag_{561}. The Ag_{55} nanoparticle was considered in detail and the multiple resonances in its response were shown to reflect the splitting of the plasmon due to the strong coupling between the plasmon and individual single-electron transitions.[106–109] In the larger Ag_{147}, Ag_{309}, and Ag_{561} nanoparticles, the interaction between plasmon and individual single-electron transitions close to the resonance is weaker and a distinct plasmon resonance emerges from the constructive superposition of low-energy Kohn–Sham transitions[39,111] accompanied by the damping due to *d*-electron transitions.[112–114]

In summary, the implemented tool raises the analysis capabilities of RT-TDDFT to the same level with the Casida approach, without compromising the computational benefits of RT-TDDFT.

Acknowledgement

We thank the Academy of Finland for support through its Centres of Excellence Programme (2012–2017) under Projects No. 251748 and No. 284621. M. K. is grateful for Academy of Finland Postdoctoral Researcher funding under Project No. 295602. T. P. R. thanks the Vilho, Yrjö and Kalle Väisälä Foundation of the Finnish Academy of Science and Letters, and Finnish Cultural Foundation for support. We also thank the Swedish Research Council, the Knut and Alice Wallenberg Foundation, and the Swedish Foundation for Strategic Research for support. We acknowledge computational resources provided by CSC – IT Center for Science (Finland), the Aalto Science-IT project (Aalto University School of Science), the Swedish National Infrastructure for Computing at NSC (Linköping) and at PDC (Stockholm).

We acknowledge the NumPy[133] and Matplotlib[134] Python packages and the VMD software,[135,136] which were used for processing the data and generating the figures.

Supporting Information Available

- supplement.pdf: Derivation of Eq. (9) within the PAW formalism and additional transition contribution maps for the Ag_{55} nanoparticle.

This information is available free of charge via the Internet at `http://pubs.acs.org`.

References

(1) Runge, E.; Gross, E. K. U. Density-Functional Theory for Time-Dependent Systems. *Phys. Rev. Lett.* **1984**, *52*, 997–1000.

(2) Hohenberg, P.; Kohn, W. Inhomogeneous Electron Gas. *Phys. Rev.* **1964**, *136*, B864–B871.

(3) Kohn, W.; Sham, L. J. Self-Consistent Equations Including Exchange and Correlation Effects. *Phys. Rev.* **1965**, *140*, A1133–A1138.

(4) Marques, M. A. L., Maitra, N. T., Nogueira, F. M. S., Gross, E. K. U., Rubio, A., Eds. *Fundamentals of Time-Dependent Density Functional Theory*; Lecture Notes in Physics; Springer, 2012; Vol. 837.

(5) Ullrich, C. A. *Time-Dependent Density-Functional Theory: Concepts and Applications*; Oxford University Press, 2012.

(6) Ekardt, W. Dynamical Polarizability of Small Metal Particles: Self-Consistent Spherical Jellium Background Model. *Phys. Rev. Lett.* **1984**, *52*, 1925–1928.

(7) Puska, M. J.; Nieminen, R. M.; Manninen, M. Electronic polarizability of small metal spheres. *Phys. Rev. B* **1985**, *31*, 3486–3495.

(8) Beck, D. E. Self-consistent calculation of the eigenfrequencies for the electronic excitations in small jellium spheres. *Phys. Rev. B* **1987**, *35*, 7325–7333.

(9) Morton, S. M.; Silverstein, D. W.; Jensen, L. Theoretical Studies of Plasmonics using Electronic Structure Methods. *Chem. Rev.* **2011**, *111*, 3962–3994.

(10) Varas, A.; García-González, P.; Feist, J.; García-Vidal, F.; Rubio, A. Quantum plasmonics: from jellium models to ab initio calculations. *Nanophotonics* **2016**, *5*, 409.

(11) Prodan, E.; Nordlander, P.; Halas, N. J. Electronic Structure and Optical Properties of Gold Nanoshells. *Nano Lett.* **2003**, *3*, 1411–1415.

(12) Aikens, C. M.; Li, S.; Schatz, G. C. From Discrete Electronic States to Plasmons: TDDFT Optical Absorption Properties of Ag_n ($n = 10, 20, 35, 56, 84, 120$) Tetrahedral Clusters. *J. Phys. Chem. C* **2008**, *112*, 11272–11279.

(13) Zuloaga, J.; Prodan, E.; Nordlander, P. Quantum Plasmonics: Optical Properties and Tunability of Metallic Nanorods. *ACS Nano* **2010**, *4*, 5269–5276.

(14) Weissker, H.-C.; Mottet, C. Optical properties of pure and core-shell noble-metal nanoclusters from TDDFT: The influence of the atomic structure. *Phys. Rev. B* **2011**, *84*, 165443.

(15) Li, J.-H.; Hayashi, M.; Guo, G.-Y. Plasmonic excitations in quantum-sized sodium nanoparticles studied by time-dependent density functional calculations. *Phys. Rev. B* **2013**, *88*, 155437.

(16) Piccini, G.; Havenith, R. W. A.; Broer, R.; Stener, M. Gold Nanowires: A Time-Dependent Density Functional Assessment of Plasmonic Behavior. *J. Phys. Chem. C* **2013**, *117*, 17196–17204.

(17) Burgess, R. W.; Keast, V. J. TDDFT Study of the Optical Absorption Spectra of Bare Gold Clusters. *J. Phys. Chem. C* **2014**, *118*, 3194–3201.

(18) Barcaro, G.; Sementa, L.; Fortunelli, A.; Stener, M. Optical Properties of Silver Nanoshells from Time-Dependent Density Functional Theory Calculations. *J. Phys. Chem. C* **2014**, *118*, 12450–12458.

(19) Weissker, H.-C.; Lopez-Lozano, X. Surface plasmons in quantum-sized noble-metal clusters: TDDFT quantum calculations and the classical picture of charge oscillations. *Phys. Chem. Chem. Phys.* **2015**, *17*, 28379–28386.

(20) Bae, G.-T.; Aikens, C. M. Time-Dependent Density Functional Theory Studies of Optical Properties of Au Nanoparticles: Octahedra, Truncated Octahedra, and Icosahedra. *J. Phys. Chem. C* **2015**, *119*, 23127–23137.

(21) Zapata Herrera, M.; Aizpurua, J.; Kazansky, A. K.; Borisov, A. G. Plasmon Response and Electron Dynamics in Charged Metallic Nanoparticles. *Langmuir* **2016**, *32*, 2829–2840.

(22) Zuloaga, J.; Prodan, E.; Nordlander, P. Quantum Description of the Plasmon Resonances of a Nanoparticle Dimer. *Nano Lett.* **2009**, *9*, 887–891.

(23) Song, P.; Nordlander, P.; Gao, S. Quantum mechanical study of the coupling of plasmon excitations to atomic-scale electron transport. *J. Chem. Phys.* **2011**, *134*, 074701.

(24) Song, P.; Meng, S.; Nordlander, P.; Gao, S. Quantum plasmonics: Symmetry-dependent plasmon-molecule coupling and quantized photoconductances. *Phys. Rev. B* **2012**, *86*, 121410.

(25) Marinica, D.; Kazansky, A.; Nordlander, P.; Aizpurua, J.; Borisov, A. G. Quantum Plasmonics: Nonlinear Effects in the Field Enhancement of a Plasmonic Nanoparticle Dimer. *Nano Lett.* **2012**, *12*, 1333–1339.

(26) Zhang, P.; Feist, J.; Rubio, A.; García-González, P.; García-Vidal, F. J. Ab initio nanoplasmonics: The impact of atomic structure. *Phys. Rev. B* **2014**, *90*, 161407.

(27) Varas, A.; García-González, P.; García-Vidal, F. J.; Rubio, A. Anisotropy Effects on the Plasmonic Response of Nanoparticle Dimers. *J. Phys. Chem. Lett.* **2015**, *6*, 1891–1898.

(28) Barbry, M.; Koval, P.; Marchesin, F.; Esteban, R.; Borisov, A. G.; Aizpurua, J.; Sánchez-Portal, D. Atomistic Near-Field Nanoplasmonics: Reaching Atomic-Scale Resolution in Nanooptics. *Nano Lett.* **2015**, *15*, 3410–3419.

(29) Kulkarni, V.; Manjavacas, A. Quantum Effects in Charge Transfer Plasmons. *ACS Photonics* **2015**, *2*, 987–992.

(30) Rossi, T. P.; Zugarramurdi, A.; Puska, M. J.; Nieminen, R. M. Quantized Evolution of the Plasmonic Response in a Stretched Nanorod. *Phys. Rev. Lett.* **2015**, *115*, 236804.

(31) Marchesin, F.; Koval, P.; Barbry, M.; Aizpurua, J.; Sánchez-Portal, D. Plasmonic Response of Metallic Nanojunctions Driven by Single Atom Motion: Quantum Transport Revealed in Optics. *ACS Photonics* **2016**, *3*, 269–277.

(32) Lahtinen, T.; Hulkko, E.; Sokolowska, K.; Tero, T.-R.; Saarnio, V.; Lindgren, J.; Pettersson, M.; Hakkinen, H.; Lehtovaara, L. Covalently linked multimers of gold nanoclusters Au_{102}(p-MBA)$_{44}$ and $Au_{\sim 250}$(p-MBA)$_n$. *Nanoscale* **2016**, *8*, 18665–18674.

(33) Manjavacas, A.; Marchesin, F.; Thongrattanasiri, S.; Koval, P.; Nordlander, P.; Sánchez-Portal, D.; García de Abajo, F. J. Tunable Molecular Plasmons in Polycyclic Aromatic Hydrocarbons. *ACS Nano* **2013**, *7*, 3635–3643.

(34) Andersen, K.; Thygesen, K. S. Plasmons in metallic monolayer and bilayer transition metal dichalcogenides. *Phys. Rev. B* **2013**, *88*, 155128.

(35) Andersen, K.; Jacobsen, K. W.; Thygesen, K. S. Plasmons on the edge of MoS_2 nanostructures. *Phys. Rev. B* **2014**, *90*, 161410.

(36) Lauchner, A.; Schlather, A. E.; Manjavacas, A.; Cui, Y.; McClain, M. J.; Stec, G. J.; García de Abajo, F. J.; Nordlander, P.; Halas, N. J. Molecular Plasmonics. *Nano Lett.* **2015**, *15*, 6208–6214.

(37) Gao, S.; Yuan, Z. Emergence of collective plasmon excitation in a confined one-dimensional electron gas. *Phys. Rev. B* **2005**, *72*, 121406.

(38) Yan, J.; Yuan, Z.; Gao, S. End and Central Plasmon Resonances in Linear Atomic Chains. *Phys. Rev. Lett.* **2007**, *98*, 216602.

(39) Bernadotte, S.; Evers, F.; Jacob, C. R. Plasmons in Molecules. *J. Phys. Chem. C* **2013**, *117*, 1863–1878.

(40) Malola, S.; Lehtovaara, L.; Enkovaara, J.; Häkkinen, H. Birth of the Localized Surface

Plasmon Resonance in Monolayer-Protected Gold Nanoclusters. *ACS Nano* **2013**, *7*, 10263–10270.

(41) Guidez, E. B.; Aikens, C. M. Theoretical analysis of the optical excitation spectra of silver and gold nanowires. *Nanoscale* **2012**, *4*, 4190–4198.

(42) Guidez, E. B.; Aikens, C. M. Quantum mechanical origin of the plasmon: from molecular systems to nanoparticles. *Nanoscale* **2014**, *6*, 11512–11527.

(43) Yasuike, T.; Nobusada, K.; Hayashi, M. Collectivity of plasmonic excitations in small sodium clusters with ring and linear structures. *Phys. Rev. A* **2011**, *83*, 013201.

(44) Casanova, D.; Matxain, J. M.; Ugalde, J. M. Plasmonic Resonances in the Al_{13}^- Cluster: Quantification and Origin of Exciton Collectivity. *J. Phys. Chem. C* **2016**, *120*, 12742–12750.

(45) Townsend, E.; Bryant, G. W. Plasmonic Properties of Metallic Nanoparticles: The Effects of Size Quantization. *Nano Lett.* **2012**, *12*, 429–434.

(46) Townsend, E.; Bryant, G. W. Which resonances in small metallic nanoparticles are plasmonic? *J. Opt.* **2014**, *16*, 114022.

(47) Ma, J.; Wang, Z.; Wang, L.-W. Interplay between plasmon and single-particle excitations in a metal nanocluster. *Nat. Commun.* **2015**, *6*, 10107.

(48) Bursi, L.; Calzolari, A.; Corni, S.; Molinari, E. Quantifying the Plasmonic Character of Optical Excitations in Nanostructures. *ACS Photonics* **2016**, *3*, 520–525.

(49) Esteban, R.; Borisov, A. G.; Nordlander, P.; Aizpurua, J. Bridging quantum and classical plasmonics with a quantum-corrected model. *Nat. Commun.* **2012**, *3*, 825.

(50) Stella, L.; Zhang, P.; García-Vidal, F. J.; Rubio, A.; García-González, P. Performance of Nonlocal Optics When Applied to Plasmonic Nanostructures. *J. Phys. Chem. C* **2013**, *117*, 8941–8949.

(51) Chen, X.; Moore, J. E.; Zekarias, M.; Jensen, L. Atomistic electrodynamics simulations of bare and ligand-coated nanoparticles in the quantum size regime. *Nat. Commun.* **2015**, *6*, 8921.

(52) Yan, W.; Wubs, M.; Asger Mortensen, N. Projected Dipole Model for Quantum Plasmonics. *Phys. Rev. Lett.* **2015**, *115*, 137403.

(53) Teperik, T. V.; Kazansky, A. K.; Borisov, A. G. Electron tunneling through water layer in nanogaps probed by plasmon resonances. *Phys. Rev. B* **2016**, *93*, 155431.

(54) Ciracì, C.; Della Sala, F. Quantum hydrodynamic theory for plasmonics: Impact of the electron density tail. *Phys. Rev. B* **2016**, *93*, 205405.

(55) David, C.; Christensen, J.; Mortensen, N. A. Spatial dispersion in two-dimensional plasmonic crystals: Large blueshifts promoted by diffraction anomalies. *Phys. Rev. B* **2016**, *94*, 165410.

(56) Christensen, T.; Yan, W.; Jauho, A.-P.; Soljačić, M.; Mortensen, N. A. Quantum Corrections in Nanoplasmonics: Shape, Scale, and Material. *Phys. Rev. Lett.* **2017**, *118*, 157402.

(57) Ciracì, C.; Hill, R. T.; Mock, J. J.; Urzhumov, Y.; Fernández-Domínguez, A. I.; Maier, S. A.; Pendry, J. B.; Chilkoti, A.; Smith, D. R. Probing the Ultimate Limits of Plasmonic Enhancement. *Science* **2012**, *337*, 1072–1074.

(58) Scholl, J. A.; Koh, A. L.; Dionne, J. A. Quantum plasmon resonances of individual metallic nanoparticles. *Nature* **2012**, *483*, 421–427.

(59) Haberland, H. Looking from both sides. *Nature* **2013**, *494*, E1–E2.

(60) Savage, K. J.; Hawkeye, M. M.; Esteban, R.; Borisov, A. G.; Aizpurua, J.; Baumberg, J. J. Revealing the quantum regime in tunnelling plasmonics. *Nature* **2012**, *491*, 574–577.

(61) Banik, M.; El-Khoury, P. Z.; Nag, A.; Rodriguez-Perez, A.; Guarrottxena, N.; Bazan, G. C.; Apkarian, V. A. Surface-Enhanced Raman Trajectories on a Nano-Dumbbell: Transition from Field to Charge Transfer Plasmons as the Spheres Fuse. *ACS Nano* **2012**, *6*, 10343–10354.

(62) Banik, M.; Apkarian, V. A.; Park, T.-H.; Galperin, M. Raman Staircase in Charge Transfer SERS at the Junction of Fusing Nanospheres. *J. Phys. Chem. Lett.* **2013**, *4*, 88–92.

(63) Scholl, J. A.; García-Etxarri, A.; Koh, A. L.; Dionne, J. A. Observation of Quantum Tunneling between Two Plasmonic Nanoparticles. *Nano Lett.* **2013**, *13*, 564–569.

(64) Tan, S. F.; Wu, L.; Yang, J. K.; Bai, P.; Bosman, M.; Nijhuis, C. A. Quantum Plasmon Resonances Controlled by Molecular Tunnel Junctions. *Science* **2014**, *343*, 1496–1499.

(65) Raza, S.; Kadkhodazadeh, S.; Christensen, T.; Di Vece, M.; Wubs, M.; Mortensen, N. A.; Stenger, N. Multipole plasmons and their disappearance in few-nanometre silver nanoparticles. *Nat. Commun.* **2015**, *6*, 8788.

(66) Zhang, C.; Zhao, H.; Zhou, L.; Schlather, A. E.; Dong, L.; McClain, M. J.; Swearer, D. F.; Nordlander, P.; Halas, N. J. Al–Pd Nanodisk Heterodimers as Antenna–Reactor Photocatalysts. *Nano Lett.* **2016**, *16*, 6677–6682.

(67) Sanders, A.; Bowman, R. W.; Baumberg, J. J. Tracking Optical and Electronic Behaviour of Quantum Contacts in Sub-Nanometre Plasmonic Cavities. *Sci. Rep.* **2016**, *6*, 32988.

(68) Mertens, J.; Demetriadou, A.; Bowman, R. W.; Benz, F.; Kleemann, M.-E.; Tserkezis, C.; Shi, Y.; Yang, H. Y.; Hess, O.; Aizpurua, J.; Baumberg, J. J. Tracking Optical Welding through Groove Modes in Plasmonic Nanocavities. *Nano Lett.* **2016**, *16*, 5605–5611.

(69) Tame, M. S.; McEnery, K. R.; Ozdemir, S. K.; Lee, J.; Maier, S. A.; Kim, M. S. Quantum plasmonics. *Nat. Phys.* **2013**, *9*, 329.

(70) Zhu, W.; Esteban, R.; Borisov, A. G.; Baumberg, J. J.; Nordlander, P.; Lezec, H. J.; Aizpurua, J.; Crozier, K. B. Quantum mechanical effects in plasmonic structures with subnanometre gaps. *Nat. Commun.* **2016**, *7*, 11495.

(71) Iida, K.; Noda, M.; Ishimura, K.; Nobusada, K. First-Principles Computational Visualization of Localized Surface Plasmon Resonance in Gold Nanoclusters. *J. Phys. Chem. A* **2014**, *118*, 11317–11322.

(72) Kuisma, M.; Sakko, A.; Rossi, T. P.; Larsen, A. H.; Enkovaara, J.; Lehtovaara, L.; Rantala, T. T. Localized surface plasmon resonance in silver nanoparticles: Atomistic first-principles time-dependent density-functional theory calculations. *Phys. Rev. B* **2015**, *91*, 115431.

(73) Baseggio, O.; Fronzoni, G.; Stener, M. A new time dependent density functional algorithm for large systems and plasmons in metal clusters. *J. Chem. Phys.* **2015**, *143*, 024106.

(74) Baseggio, O.; De Vetta, M.; Fronzoni, G.; Stener, M.; Sementa, L.; Fortunelli, A.; Calzolari, A. Photoabsorption of Icosahedral Noble Metal Clusters: An Efficient TDDFT Approach to Large-Scale Systems. *J. Phys. Chem. C* **2016**, *120*, 12773–12782.

(75) Koval, P.; Marchesin, F.; Foerster, D.; Sánchez-Portal, D. Optical response of silver clusters and their hollow shells from linear-response TDDFT. *J. Phys.: Condens. Matter* **2016**, *28*, 214001.

(76) Casida, M. E. In *Recent Advances in Density Functional Methods, Part I*; Chong, D. P., Ed.; World Scientific, Singapore, 1995; p 155.

(77) Petersilka, M.; Gossmann, U. J.; Gross, E. K. U. Excitation Energies from Time-Dependent Density-Functional Theory. *Phys. Rev. Lett.* **1996**, *76*, 1212–1215.

(78) Casida, M. E. Time-dependent density-functional theory for molecules and molecular solids. *J. Mol. Struct.: THEOCHEM* **2009**, *914*, 3–18.

(79) Bauernschmitt, R.; Ahlrichs, R. Treatment of electronic excitations within the adiabatic approximation of time dependent density functional theory. *Chem. Phys. Lett.* **1996**, *256*, 454–464.

(80) Stratmann, R. E.; Scuseria, G. E.; Frisch, M. J. An efficient implementation of time-dependent density-functional theory for the calculation of excitation energies of large molecules. *J. Chem. Phys.* **1998**, *109*, 8218–8224.

(81) Walker, B.; Saitta, A. M.; Gebauer, R.; Baroni, S. Efficient Approach to Time-Dependent Density-Functional Perturbation Theory for Optical Spectroscopy. *Phys. Rev. Lett.* **2006**, *96*, 113001.

(82) Andrade, X.; Botti, S.; Marques, M. A. L.; Rubio, A. Time-dependent density functional theory scheme for efficient calculations of dynamic (hyper)polarizabilities. *J. Chem. Phys.* **2007**, *126*, 184106.

(83) Yabana, K.; Bertsch, G. F. Time-dependent local-density approximation in real time. *Phys. Rev. B* **1996**, *54*, 4484–4487.

(84) Yabana, K.; Nakatsukasa, T.; Iwata, J.-I.; Bertsch, G. F. Real-time, real-space implementation of the linear response time-dependent density-functional theory. *Phys. Status Solidi B* **2006**, *243*, 1121–1138.

(85) Sander, T.; Kresse, G. Macroscopic dielectric function within time-dependent density functional theory—Real time evolution versus the Casida approach. *J. Chem. Phys.* **2017**, *146*, 064110.

(86) Malola, S.; Lehtovaara, L.; Häkkinen, H. TDDFT Analysis of Optical Properties of Thiol Monolayer-Protected Gold and Intermetallic Silver–Gold $Au_{144}(SR)_{60}$ and $Au_{84}Ag_{60}(SR)_{60}$ Clusters. *J. Phys. Chem. C* **2014**, *118*, 20002–20008.

(87) Malola, S.; Hartmann, M. J.; Häkkinen, H. Copper Induces a Core Plasmon in Intermetallic $Au_{(144,145)-x}Cu_x(SR)_{60}$ Nanoclusters. *J. Phys. Chem. Lett.* **2015**, *6*, 515–520.

(88) Nadler, R.; Sanz, J. F. Simulating the optical properties of CdSe clusters using the RT-TDDFT approach. *Theor. Chem. Acc.* **2013**, *132*, 1342.

(89) Hofmann, D.; Kümmel, S. Self-interaction correction in a real-time Kohn-Sham scheme: Access to difficult excitations in time-dependent density functional theory. *J. Chem. Phys.* **2012**, *137*, 064117.

(90) Hu, C.; Sugino, O.; Miyamoto, Y. Modified linear response for time-dependent density-functional theory: Application to Rydberg and charge-transfer excitations. *Phys. Rev. A* **2006**, *74*, 032508.

(91) Quijada, M.; Muiño, R. D.; Borisov, A. G.; Alonso, J. A.; Echenique, P. M. Lifetime of electronic excitations in metal nanoparticles. *New J. Phys.* **2010**, *12*, 053023.

(92) Yan, L.; Wang, F.; Meng, S. Quantum Mode Selectivity of Plasmon-Induced Water Splitting on Gold Nanoparticles. *ACS Nano* **2016**, *10*, 5452–5458.

(93) Li, X.; Smith, S. M.; Markevitch, A. N.; Romanov, D. A.; Levis, R. J.; Schlegel, H. B. A time-dependent Hartree-Fock approach for studying the electronic optical response of molecules in intense fields. *Phys. Chem. Chem. Phys.* **2005**, *7*, 233–239.

(94) Ding, F.; Guidez, E. B.; Aikens, C. M.; Li, X. Quantum coherent plasmon in silver nanowires: A real-time TDDFT study. *J. Chem. Phys.* **2014**, *140*, 244705.

(95) Bende, A.; Tosa, V. Modeling laser induced molecule excitation using real-time time-dependent density functional theory: application to 5- and 6-benzyluracil. *Phys. Chem. Chem. Phys.* **2015**, *17*, 5861–5871.

(96) Provorse, M. R.; Habenicht, B. F.; Isborn, C. M. Peak-Shifting in Real-Time Time-Dependent Density Functional Theory. *J. Chem. Theory Comput.* **2015**, *11*, 4791–4802.

(97) Repisky, M.; Konecny, L.; Kadek, M.; Komorovsky, S.; Malkin, O. L.; Malkin, V. G.; Ruud, K. Excitation Energies from Real-Time Propagation of the Four-Component Dirac–Kohn–Sham Equation. *J. Chem. Theory Comput.* **2015**, *11*, 980–991.

(98) Bruner, A.; LaMaster, D.; Lopata, K. Accelerated Broadband Spectra Using Transition Dipole Decomposition and Padé Approximants. *J. Chem. Theory Comput.* **2016**, *12*, 3741–3750.

(99) Li, Y.; Ullrich, C. A. Time-dependent transition density matrix. *Chem. Phys.* **2011**, *391*, 157–163.

(100) Li, Y.; Ullrich, C. A. The Particle–Hole Map: A Computational Tool To Visualize Electronic Excitations. *J. Chem. Theory Comput.* **2015**, *11*, 5838–5852.

(101) Kolesov, G.; Grånäs, O.; Hoyt, R.; Vinichenko, D.; Kaxiras, E. Real-Time TD-DFT with Classical Ion Dynamics: Methodology and Applications. *J. Chem. Theory Comput.* **2016**, *12*, 466–476.

(102) Mortensen, J. J.; Hansen, L. B.; Jacobsen, K. W. Real-space grid implementation of the projector augmented wave method. *Phys. Rev. B* **2005**, *71*, 035109.

(103) Enkovaara, J.; Rostgaard, C.; Mortensen, J. J.; Chen, J.; Dułak, M.; Ferrighi, L.; Gavnholt, J.; Glinsvad, C.; Haikola, V.; Hansen, H. A.; Kristoffersen, H. H.; Kuisma, M.; Larsen, A. H.; Lehtovaara, L.; Ljungberg, M.; Lopez-Acevedo, O.;

Moses, P. G.; Ojanen, J.; Olsen, T.; Petzold, V.; Romero, N. A.; Stausholm-Møller, J.; Strange, M.; Tritsaris, G. A.; Vanin, M.; Walter, M.; Hammer, B.; Häkkinen, H.; Madsen, G. K. H.; Nieminen, R. M.; Nørskov, J. K.; Puska, M.; Rantala, T. T.; Schiøtz, J.; Thygesen, K. S.; Jacobsen, K. W. Electronic structure calculations with GPAW: a real-space implementation of the projector augmented-wave method. *J. Phys.: Condens. Matter* **2010**, *22*, 253202.

(104) GPAW: DFT and beyond within the projector-augmented wave method. `https://wiki.fysik.dtu.dk/gpaw` (accessed June 1, 2017).

(105) Larsen, A. H.; Vanin, M.; Mortensen, J. J.; Thygesen, K. S.; Jacobsen, K. W. Localized atomic basis set in the projector augmented wave method. *Phys. Rev. B* **2009**, *80*, 195112.

(106) Ekardt, W. Size-dependent photoabsorption and photoemission of small metal particles. *Phys. Rev. B* **1985**, *31*, 6360–6370.

(107) Yannouleas, C.; Broglia, R. A.; Brack, M.; Bortignon, P. F. Fragmentation of the photoabsorption strength in neutral and charged metal microclusters. *Phys. Rev. Lett.* **1989**, *63*, 255–258.

(108) Penzar, Z.; Ekardt, W.; Rubio, A. Temperature effects on the optical absorption of jellium clusters. *Phys. Rev. B* **1990**, *42*, 5040–5045.

(109) Yannouleas, C.; Broglia, R. A. Collective and single-particle aspects in the optical response of metal microclusters. *Phys. Rev. A* **1991**, *44*, 5793–5802.

(110) Pines, D.; Bohm, D. A Collective Description of Electron Interactions: II. Collective vs Individual Particle Aspects of the Interactions. *Phys. Rev.* **1952**, *85*, 338–353.

(111) Yannouleas, C.; Broglia, R. Landau damping and wall dissipation in large metal clusters. *Ann. Phys.* **1992**, *217*, 105–141.

(112) Liebsch, A. Surface plasmon dispersion of Ag. *Phys. Rev. Lett.* **1993**, *71*, 145–148.

(113) Liebsch, A. Surface-plasmon dispersion and size dependence of Mie resonance: Silver versus simple metals. *Phys. Rev. B* **1993**, *48*, 11317–11328.

(114) Tiggesbäumker, J.; Köller, L.; Meiwes-Broer, K.-H.; Liebsch, A. Blue shift of the Mie plasma frequency in Ag clusters and particles. *Phys. Rev. A* **1993**, *48*, R1749–R1752.

(115) Bahn, S.; Jacobsen, K. An object-oriented scripting interface to a legacy electronic structure code. *Comput. Sci. Eng.* **2002**, *4*, 56–66.

(116) Larsen, A.; Mortensen, J.; Blomqvist, J.; Castelli, I.; Christensen, R.; Dulak, M.; Friis, J.; Groves, M.; Hammer, B.; Hargus, C.; Hermes, E.; Jennings, P.; Jensen, P.; Kermode, J.; Kitchin, J.; Kolsbjerg, E.; Kubal, J.; Kaasbjerg, K.; Lysgaard, S.; Maronsson, J.; Maxson, T.; Olsen, T.; Pastewka, L.; Peterson, A.; Rostgaard, C.; Schiøtz, J.; Schütt, O.; Strange, M.; Thygesen, K.; Vegge, T.; Vilhelmsen, L.; Walter, M.; Zeng, Z.; Jacobsen, K. W. The Atomic Simulation Environment – A Python library for working with atoms. *J. Phys.: Condens. Matter* **2017**, *29*, 273002.

(117) Blöchl, P. E. Projector augmented-wave method. *Phys. Rev. B* **1994**, *50*, 17953–17979.

(118) Friedrichi, H. *Theoretical Atomic Physics, Third edition*; Springer Berlin Heidelberg, 2006.

(119) Walter, M.; Häkkinen, H.; Lehtovaara, L.; Puska, M.; Enkovaara, J.; Rostgaard, C.; Mortensen, J. J. Time-dependent density-functional theory in the projector augmented-wave method. *J. Chem. Phys.* **2008**, *128*, 244101.

(120) Wilkinson, P. G. Absorption spectra of benzene and benzene-d_6 in the vacuum ultraviolet. *Can. J. Phys.* **1956**, *34*, 596–615.

(121) Ferguson, J.; Reeves, L. W.; Schneider, W. G. Vapor absorption spectra and oscillator

strengths of naphthalene, anthracene, and pyrene. *Can. J. Chem.* **1957**, *35*, 1117–1136.

(122) Rossi, T. P.; Lehtola, S.; Sakko, A.; Puska, M. J.; Nieminen, R. M. Nanoplasmonics simulations at the basis set limit through completeness-optimized, local numerical basis sets. *J. Chem. Phys.* **2015**, *142*, 094114.

(123) (a) Perdew, J. P.; Burke, K.; Ernzerhof, M. Generalized Gradient Approximation Made Simple. *Phys. Rev. Lett.* **1996**, *77*, 3865–3868; (b) Perdew, J. P.; Burke, K.; Ernzerhof, M. Generalized Gradient Approximation Made Simple [Phys. Rev. Lett. 77, 3865 (1996)]. *Phys. Rev. Lett.* **1997**, *78*, 1396–1396.

(124) The timing was performed on the Taito supercluster of CSC – IT Center for Science, Finland. Each computing node has Intel Haswell E5-2690v3 processors and the nodes are connected with Infiniband FDR interconnect. For further details of the hardware, see `https://research.csc.fi/taito-supercluster` (accessed June 1, 2017).

(125) Gritsenko, O.; van Leeuwen, R.; van Lenthe, E.; Baerends, E. J. Self-consistent approximation to the Kohn-Sham exchange potential. *Phys. Rev. A* **1995**, *51*, 1944–1954.

(126) Kuisma, M.; Ojanen, J.; Enkovaara, J.; Rantala, T. T. Kohn-Sham potential with discontinuity for band gap materials. *Phys. Rev. B* **2010**, *82*, 115106.

(127) Yan, J.; Jacobsen, K. W.; Thygesen, K. S. First-principles study of surface plasmons on Ag(111) and H/Ag(111). *Phys. Rev. B* **2011**, *84*, 235430.

(128) Yan, J.; Jacobsen, K. W.; Thygesen, K. S. Conventional and acoustic surface plasmons on noble metal surfaces: A time-dependent density functional theory study. *Phys. Rev. B* **2012**, *86*, 241404.

(129) He, Y.; Zeng, T. First-Principles Study and Model of Dielectric Functions of Silver Nanoparticles. *J. Phys. Chem. C* **2010**, *114*, 18023–18030.

(130) Krauter, C. M.; Bernadotte, S.; Jacob, C. R.; Pernpointner, M.; Dreuw, A. Identification of Plasmons in Molecules with Scaled Ab Initio Approaches. *J. Phys. Chem. C* **2015**, *119*, 24564–24573.

(131) Bae, G.-T.; Aikens, C. M. Time-Dependent Density Functional Theory Studies of Optical Properties of Ag Nanoparticles: Octahedra, Truncated Octahedra, and Icosahedra. *J. Phys. Chem. C* **2012**, *116*, 10356–10367.

(132) Rabilloud, F. Description of plasmon-like band in silver clusters: The importance of the long-range Hartree-Fock exchange in time-dependent density-functional theory simulations. *J. Chem. Phys.* **2014**, *141*, 144302.

(133) van der Walt, S.; Colbert, S. C.; Varoquaux, G. The NumPy Array: A Structure for Efficient Numerical Computation. *Comput. Sci. Eng.* **2011**, *13*, 22.

(134) Hunter, J. D. Matplotlib: A 2D graphics environment. *Comput. Sci. Eng.* **2007**, *9*, 90–95.

(135) Humphrey, W.; Dalke, A.; Schulten, K. VMD – Visual Molecular Dynamics. *J. Mol. Graph.* **1996**, *14*, 33.

(136) Stone, J. An Efficient Library for Parallel Ray Tracing and Animation. M.Sc. thesis, Computer Science Department, University of Missouri-Rolla, 1998.

Graphical TOC Entry